

See discussions, stats, and author profiles for this publication at: <https://www.researchgate.net/publication/231240093>

# Aerosol-Assisted Synthesis of Magnetic Mesoporous Silica Spheres for Drug Targeting

ARTICLE in CHEMISTRY OF MATERIALS · JUNE 2007

Impact Factor: 8.35 · DOI: 10.1021/cm0705789

CITATIONS

111

READS

54

6 AUTHORS, INCLUDING:



**Eduardo Ruiz-Hernandez**

Utrecht University

27 PUBLICATIONS 854 CITATIONS

SEE PROFILE



**Daniel Arcos**

Complutense University of Madrid

89 PUBLICATIONS 3,560 CITATIONS

SEE PROFILE



**Isabel Izquierdo-Barba**

Complutense University of Madrid

86 PUBLICATIONS 3,131 CITATIONS

SEE PROFILE



**Osamu Terasaki**

Stockholm University

450 PUBLICATIONS 21,283 CITATIONS

SEE PROFILE

# Aerosol-Assisted Synthesis of Magnetic Mesoporous Silica Spheres for Drug Targeting

E. Ruiz-Hernández,<sup>†</sup> A. López-Noriega,<sup>†</sup> D. Arcos,<sup>†</sup> I. Izquierdo-Barba,<sup>‡,§</sup> O. Terasaki,<sup>‡</sup> and M. Vallet-Regí<sup>\*,†</sup>

*Departamento de Química Inorgánica y Bioinorgánica, Facultad de Farmacia, Universidad Complutense de Madrid, 28040, Madrid, Spain, and Structural Chemistry, Arrhenius Laboratory, Stockholm University, S-10691 Stockholm, Sweden*

*Received March 1, 2007. Revised Manuscript Received April 12, 2007*

Spherical silica-based mesoporous materials encapsulating magnetic nanoparticles have been synthesized following an aerosol-assisted route. The influence of nonionic surfactant P123 concentration in the structural and textural parameters has been investigated. Moreover, the effect of adding different amounts of magnetic nanoparticles to the precursor solution has been studied attending to structural, textural, and magnetic properties. The ability of these materials to achieve stability in aqueous solution at physiological pH, and their potential to be magnetically guided, have been evaluated. The microspheres adsorption and release performance have been tested by using ibuprofen as a model drug.

## Introduction

Silica mesoporous materials have been intensively investigated for the past 15 years.<sup>1,2</sup> Several applications have been proposed in the fields of catalysis, lasers, sensors, solar cells, etc.,<sup>3–8</sup> implying their superior adsorption capacities. In the biomedical field, drug delivery has been presented as a potential use of these structures,<sup>9</sup> due to different features: among others, a suitable pore size to host biomolecules, high specific surface areas, and the ability to be easily functionalized.<sup>10–15</sup>

Magnetic nanoparticles have also been the focus of many researchers because of their broad range of possible

applications<sup>16–23</sup> in electronics, catalysis, magnetic memories, and biomedicine. The latter includes aspects such as magnetic bioseparations,<sup>24,25</sup> hyperthermia of tumors,<sup>26</sup> retinal detachment therapy,<sup>27</sup> enhancement of contrast agents for magnetic resonance imaging,<sup>28,29</sup> and drug carriers design.<sup>30–32</sup> Magnetic nanoparticles as drug delivery vectors provide the ability to selectively target the desired organs or tissues inside the body, as well as accumulate a certain concentration of nanoparticles along the therapy path by means of the application of an external magnetic field.<sup>33</sup>

Most of the materials designed for drug targeting purposes are based on core–shell nanoparticles, where magnetic

\* Corresponding author.

<sup>†</sup> Universidad Complutense de Madrid.

<sup>‡</sup> Stockholm University.

<sup>§</sup> Permanent address: Departamento de Química Inorgánica y Bioinorgánica, Facultad de Farmacia, Universidad Complutense de Madrid, 28040, Madrid, Spain.

- (1) Kresge, C. T.; Leonowicz, M. E.; Roth, W. J.; Vartuli, J. C.; Beck, J. S. *Nature* **1992**, *359*, 710.
- (2) Beck, J. S.; Vartuli, J. C.; Roth, W. J.; Leonowicz, M. E.; Kresge, C. T.; Schmitt, K. D.; Chu, C. T. W.; Olson, D. H.; Sheppard, E. W.; McCullen, S. B.; Higgins, J. B.; Schlenker, J. L. *J. Am. Chem. Soc.* **1992**, *114*, 10834.
- (3) Ying, J. Y.; Mehnert, P.; Wong, M. S. *Angew. Chem., Int. Ed.* **1999**, *38*, 56.
- (4) Brinker, C. J. *Curr. Opin. Solid State Mater. Sci.* **1996**, *1*, 798.
- (5) Sayari, A. *Chem. Mater.* **1996**, *8*, 1840.
- (6) Yang, H.; Kuperman, A.; Coombs, N.; Mamiche-Afara, S.; Ozin, G. A. *Nature* **1996**, *379*, 703.
- (7) Davis, M. E. *Nature* **2002**, *417*, 813.
- (8) Stein, A. *Adv. Mater.* **2003**, *15*, 763.
- (9) Vallet-Regí, M.; Rámila, A.; Del Real, R. P.; Pérez-Pariente, J. *Chem. Mater.* **2001**, *13*, 308.
- (10) Vallet-Regí, M. *Chem. Eur. J.* **2006**, *12*, 5934.
- (11) Vallet-Regí, M. *Dalton Trans.* **2006**, *44*, 5211.
- (12) Muñoz, B.; Rámila, A.; Pérez-Pariente, J.; Díaz, I.; Vallet-Regí, M. *Chem. Mater.* **2003**, *15*, 500.
- (13) Doadrio, A. L.; Sousa, E. M. B.; Doadrio, J. C.; Pérez-Pariente, J.; Izquierdo-Barba, I.; Vallet-Regí, M. *J. Controlled Release* **2004**, *97*, 125.
- (14) Salonen, J.; Laitinen, L.; Kaukonen, A. M.; Tuura, J.; Björkqvist, M.; Heikkilä, T.; Vähä-Heikkilä, K.; Hirvonen, J.; Lehto, V.-P. *J. Controlled Release* **2005**, *108*, 362.
- (15) Yang, Q.; Wang, S. H.; Fan, P. W.; Wang, L. F.; Di, Y.; Lin, K. F.; Xiao, F. S. *Chem. Mater.* **2005**, *17*, 5999.

- (16) Gass, J.; Poddar, P.; Almand, J.; Srinath, S.; Srikanth, H. *Adv. Funct. Mater.* **2006**, *16*, 71.
- (17) Yi, D. K.; Lee, S. S.; Ying, J. Y. *Chem. Mater.* **2006**, *18*, 2459.
- (18) Speliotis, D. E. *J. Magn. Magn. Mater.* **1999**, *193*, 29.
- (19) Pankhurst, Q. A.; Connolly, J.; Jones, S. K.; Dobson, J. *J. Phys. D: Appl. Phys.* **2003**, *36*, R167.
- (20) Ito, A.; Shinkai, M.; Honda, H.; Kobayashi, T. *J. Biosci. Bioeng.* **2005**, *100*, 1.
- (21) Gupta, A. K.; Gupta, M. *Biomaterials* **2005**, *26*, 3995.
- (22) Berry, C. C.; Curtis, A. S. G. *J. Phys. D: Appl. Phys.* **2003**, *36*, R198.
- (23) Mornet, S.; Vasseur, S.; Grasset, F.; Duguet, E. *J. Mater. Chem.* **2004**, *14*, 2161.
- (24) Mura, C. V.; Becker, M. I.; Orellana, A.; Wolff, D. *J. Immunol. Methods* **2002**, *260*, 263.
- (25) Kularatne, B. Y.; Lorigan, P.; Browne, S.; Suvarna, S. K.; Smith, M. O.; Lawry, J. *Cytometry* **2002**, *50*, 160.
- (26) Jordan, A.; Scholz, R.; Wust, P.; Schirra, H.; Schiestel, T.; Schmidt, H.; Felix, R. *J. Magn. Magn. Mater.* **1999**, *194*, 185.
- (27) Dailey, J. P.; Phillips, J. P.; Li, C.; Riffle, J. S. *J. Magn. Magn. Mater.* **1999**, *194*, 140.
- (28) Mornet, S.; Portier, J.; Duguet, E. *J. Magn. Magn. Mater.* **2005**, *293*, 127.
- (29) Halavaara, J.; Tervahartiala, P.; Isoniemi, H.; Höckerstedt, K. *Acta Radiol.* **2002**, *43*, 180.
- (30) Senyei, A.; Widder, K.; Czerlinski, G. *J. Appl. Phys.* **1978**, *49*, 3578.
- (31) Alexiou, C.; Arnold, W.; Klein, R. J.; Parak, F. G.; Hulin, P.; Bergemann, C.; Erhardt, W.; Wagenpfeil, S.; Lütke, A. S. *Cancer Res.* **2000**, *60*, 6641.
- (32) Widder, K. J.; Senyei, A. E.; Ranney, D. F. *Cancer Res.* **1980**, *40*, 3512.
- (33) Lütke, A.; Bergemann, C.; Brock, J.; McClure, D. G. *J. Magn. Magn. Mater.* **1999**, *194*, 149.

nanocrystals are coated by diverse species (silica,<sup>34</sup> surfactant polymers,<sup>35–37</sup> and nonpolymeric organic stabilizers<sup>38,39</sup>) aimed to avoiding contact between the magnetic core and the tissue while maintaining the colloidal suspension stability within the biological environment. A few attempts have considered the combination of mesoporous silica with magnetic nanoparticles.<sup>40–44</sup> Mesoporous materials obtained by conventional methods exhibit irregular bulk morphology.<sup>45</sup> In contrast, microspheres are widely accepted, from a clinical point of view, as useful drug delivery systems because they can be ingested or injected and present a homogeneous morphology.<sup>46–49</sup> As a result, mesoporous materials in the form of microspheres with a magnetic component represent a significant advance in the field of drug delivery. On the one hand, the outstanding textural properties of mesoporous materials allow a great load of drug and a controlled release. On the other hand, the magnetic properties allow not only the targeting or accumulation of drug in a desired place of the body but also the possibility of using hyperthermia combined with drugs for the treatment of cancerous diseases.

In this work, we present an aerosol-assisted route to synthesize mesoporous silica microspheres encapsulating magnetic nanoparticles. Some of the parameters influencing this synthesis, like surfactant concentration or the amount of embedded nanoparticles, are investigated.

## Experimental Section

A series of different silica mesoporous magnetic spheres (MMS) containing maghemite ( $\gamma$ -Fe<sub>2</sub>O<sub>3</sub>) nanoparticles were synthesized following an aerosol route, which is based on the evaporation-induced self-assembly (EISA) method.<sup>50</sup> The surfactant/silica precursor ratio was varied. This ratio (wt %) was fixed to 0, 10, 20, 25, 33, 50, 70, and 100. These samples were denoted as MMS0, MMS10, MMS20, MMS25, and so on consecutively. The content of  $\gamma$ -Fe<sub>2</sub>O<sub>3</sub> in the final materials of this series was theoretically set

to 11 wt % by the addition of ferrofluid with a well-known concentration.

To study the influence of the presence of magnetic nanoparticles inside the mesoporous network, another series of mesoporous spheres was synthesized from the MMS25 sample by varying the  $\gamma$ -Fe<sub>2</sub>O<sub>3</sub>/SiO<sub>2</sub> ratio in the final composition. This weight ratio was fixed to 0, 11, 25, and 46; these samples were denoted as MMS25-(0), MMS25(11), and so on. In this series, the surfactant/silica precursor ratio was kept constant and equal to 25.

The silica source used was tetraethoxysilane [(Si(OCH<sub>2</sub>CH<sub>3</sub>)<sub>4</sub>], TEOS) and the structure-directing agent an amphiphilic triblock copolymer, Pluronic P123 [(ethylene oxide, EO)<sub>20</sub>(propylene oxide, PO)<sub>70</sub>(EO)<sub>20</sub>], obtained as a gift from BASF. A ferrofluid based on a stable suspension of magnetic nanoparticles of  $\gamma$ -Fe<sub>2</sub>O<sub>3</sub> in water was used to incorporate the nanoparticles into the mesoporous silica matrix.

**Preparation of the Ferrofluid.** The coprecipitation of Fe(II) and Fe(III) chlorides with ammonium hydroxide at pH 9.5 was carried out, according to Massart's method,<sup>51</sup> yielding nanometric magnetite (Fe<sub>3</sub>O<sub>4</sub>). Following dispersion in 2 M HNO<sub>3</sub>, the particles were oxidized to maghemite by the addition of iron nitrate and heating at 90 °C for 30 min. After that, the product was washed with acetone several times and finally dispersed in water to a concentration of 26 g·mL<sup>-1</sup> (as measured by titration with K<sub>2</sub>Cr<sub>2</sub>O<sub>7</sub>). The ferrofluid so-obtained was composed of magnetic nanoparticles with an average diameter of 8 nm at pH 2.5, as measured by dynamic light scattering.

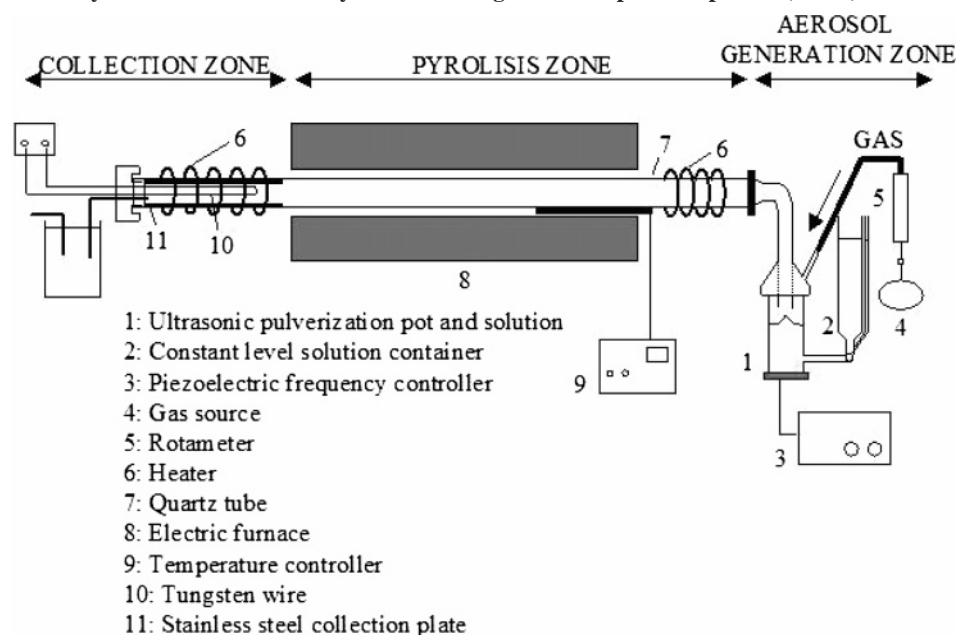
**Synthesis of the Precursor Solution.** In a typical preparation, a certain amount of Pluronic P123 was dissolved in a solution of 900 mL of ethanol and 51.13 mL of the ferrofluid. The pH of the mixture was adjusted to 1.2 by means of 4 mL of 6 M HNO<sub>3</sub>. After 3 h of stirring, 43.44 mL of TEOS was added to the solution, which was kept stirring overnight. In those samples synthesized without magnetic nanoparticles, the ferrofluid was replaced by 51.13 mL of distilled water. In the case of materials with a higher content in  $\gamma$ -Fe<sub>2</sub>O<sub>3</sub> nanoparticles, more concentrated ferrofluids were added, to maintain the amount of water as a constant in the synthesis.

**Fabrication of the Spheres.** MMS were synthesized by pyrolysis of an aerosol generated by ultra-high-frequency spraying of the solution, following a technique addressed before.<sup>52–57</sup> The processing equipment is shown in Scheme 1. A piezoelectric ceramic that allows the carrier gas flow to be freely adjusted is located at the bottom of a vessel, which contains the precursor solution of the material. When the piezoelectric transducer is excited near its own resonance frequency (about 850 kHz for the transducer used), a geyser is formed at the surface of the liquid. This geyser produces ultrafine droplets, which form an aerosol. N<sub>2</sub> gas is used as the carrier to convey the aerosol to the pyrolysis zone, which consists of a 65 cm long tubular furnace at 400 °C. The residence time of the particles in the high-temperature zone (in our case, 2 s) is controlled by the gas flow, which was fixed to 8 L·min<sup>-1</sup>. Around 1 g/h of dried particles is collected outside the furnace with an

- (34) Philipse, A. P.; Van Bruggen, M. P. B.; Pathmamanoharan, C. *Langmuir* **1994**, *10*, 92.
- (35) Jain, T. K.; Morales, M. A.; Sahoo, S. K.; Leslie-Pelecky, D. L.; Labhasetwar, V. *Mol. Pharmacol.* **2005**, *2*, 194.
- (36) Okassa, L. N.; Marchais, H.; Douziche-Eyroller, L.; Cohen-Jonathan, S.; Soucé, M.; Dubois, P.; Chourpa, I. *Int. J. Pharm.* **2005**, *302*, 187.
- (37) Cheng, J.; Teply, B. A.; Jeong, S. Y.; Yim, C. H.; Ho, D.; Sherifi, I.; Jon, S.; Farokhzad, O. C.; Khademhosseini, A.; Langer, R. S. *Pharm. Res.* **2006**, *23*, 557.
- (38) Yee, C.; Kataby, G.; Ulman, A.; Prozorov, T.; White, H.; King, A.; Rafailovich, M.; Sokolov, J.; Gedanken, A. *Langmuir* **1999**, *15*, 7111.
- (39) Portet, D.; Denizot, B.; Rump, E.; Lejeune, J. J.; Jallet, P. *J. Colloid Interface Sci.* **2001**, *238*, 37.
- (40) Giri, S.; Trewyn, B. G.; Stellmaker, M. P.; Lin, V. S.-Y. *Angew. Chem., Int. Ed.* **2005**, *44*, 5038.
- (41) Lin, Y.-S.; Hung, Y.; Su, J.-K.; Lee, R.; Chang, C.; Lin, M.-L.; Mou, C.-Y. *J. Phys. Chem. B* **2004**, *108*, 15608.
- (42) Zhao, W.; Gu, J.; Zhang, L.; Chen, H.; Shi, J. *J. Am. Chem. Soc.* **2005**, *127*, 8916.
- (43) Jaeyun, K.; Lee, J. E.; Lee, J.; Yu, H. J.; Kim, B. C.; An, K.; Hwang, Y.; Shin, C.-H.; Park, J.-G.; Kim, J.; Hyeon, T. *J. Am. Chem. Soc.* **2005**, *128*, 688.
- (44) Lin, Y.-S.; Wu, S.-H.; Hung, Y.; Chou, Y.-H.; Chang, C.; Lin, M.-L.; Tsai, C.-P.; Mou, C.-Y. *Chem. Mater.* **2006**, *18*, 5170.
- (45) Zhu, Y.-F.; Shi, J.-L.; Li, Y.-S.; Chen, H.-R.; Shen, W.-H.; Dong, X.-P. *Microporous Mesoporous Mater.* **2005**, *85*, 75.
- (46) Vasir, J. K.; Tambwekar, K.; Garg, S. *Int. J. Pharm.* **2003**, *255*, 13.
- (47) Edlund, U.; Albertsson, A. C. *Adv. Polym. Sci.* **2002**, *157*, 67.
- (48) Kawaguchi, H. *Prog. Polym. Sci.* **2000**, *25*, 1171.
- (49) Freiberg, S.; Zhu, X. X. *Int. J. Pharm.* **2004**, *282*, 1.
- (50) Brinker, C. J.; Lu, Y.; Sellinger, A.; Fan, H. *Adv. Mater.* **1999**, *11* (7), 579.

- (51) Massart, R. *IEEE Trans. Magn.* **1981**, *17*, 1247.
- (52) Tang, Z. X.; Natis, S.; Sorensen, C. M.; Hadjipanayis, G. C.; Kablunde, K. J. *J. Magn. Magn. Mater.* **1989**, *80*, 285.
- (53) Kalzmarek, W. A.; Ninham, B. W.; Calka, A. *J. Appl. Phys.* **1991**, *70*, 5909.
- (54) Vallet-Regí, M.; Gutiérrez-Ríos, M. T.; Alonso, M. P.; De Frutos, M. I.; Nicolopoulos, S. *J. Solid State Chem.* **1994**, *112*, 58.
- (55) Vallet-Regí, M. Preparative strategies for controlling structure and morphology of metal oxides. In *Perspectives in Solid State Chemistry*; Rao, K. J., Ed.; John Wiley & Sons: New York, 1995, Vol. 37.
- (56) Martínez, A.; Peña, J.; Labeau, M.; González-Calbet, J. M.; Vallet-Regí, M. *J. Mater. Res.* **1995**, *10*, 1307.
- (57) Cabañas, M. V.; Vallet-Regí, M.; Labeau, M.; González-Calbet, J. M. *J. Mater. Res.* **1993**, *8*, 2694.

Scheme 1. Laboratory-Scale Device for the Synthesis of Magnetic Mesoporous Spheres (MMS) from Aerosol Droplets



electrostatic filter, consisting of a thin tungsten wire suspended in the center of a tubular stainless steel collection plate. This wire is negatively charged with 8 kV; thus, the particles become charged and are collected on the plate. This electrostatic collection system permits a nonstop synthesis. All of the transport zone of the aerosol is kept at 100 °C so that ethanol condensation is avoided.

The system is designed in such a way that the mesostructure is mainly formed during the droplet drying at the preheating site (indicated as point 6 in Scheme 1). The temperature at this site is around 100 °C (drying zone) and the furnace is set at 400 °C to avoid the particles coalescence on the collection surface.

To remove the surfactant, the powder obtained by the aerosol-assisted method was calcined in air at 425 °C for 3 h.

**In Vitro Drug Release Essay.** A certain amount of the material synthesized with 25% P123/TEOS (denoted as MMS25(11)) was added into a pentane solution of ibuprofen (40 mg·mL<sup>-1</sup>), where it was stirred strongly for 24 h at room temperature while the evaporation of the pentane was prevented. The material was gently washed with pentane after the loading. After the loaded MMS25(11) was dried at 40 °C for 24 h, 75 mg was compacted by uniaxial pressing (0.1 ton for 1 min) and immersed into 7.5 mL of filtered simulated body fluid (SBF<sup>58</sup>) at 37 °C under stirring at 100 rpm. Samples of 1 mL were removed at given time intervals, diluted to 5 mL with SBF, and analyzed by UV-vis spectroscopy at a wavelength of 264 nm. The volume removed was replaced with the same amount of preheated filtered SBF. The experiment was carried out in triplicate.

The determination of the ibuprofen loading in the material was carried out by thermogravimetric (TG) analyses using a Seiko Thermobalance TG/DTA 320, as well as CHN elemental microanalyses.

**Characterization.** Powder X-ray diffraction (XRD) experiments were performed with a Philips X'Pert diffractometer equipped with Cu K $\alpha$  radiation (wavelength 1.5406 Å). XRD patterns were collected in the 2 $\theta$  ranges between 0.6° and 4° and between 10° and 70° with a step size of 0.02° and counting time of 5 and 10 s per step, respectively. The textural properties of the materials were determined by nitrogen sorption porosimetry by using a Micromer-

itics ASAP 2010. To perform the N<sub>2</sub> measurements, the samples were previously degassed under vacuum for 24 h at 120 °C.

Transmission electron microscopy (TEM) was carried out with a JEOL JEM 2000 FX instrument operated at 200 kV equipped with a LINK AN 10000 analytical system and CCD camera (KeenView Camera). Fourier patterns were conducted using the CRISP program. Samples preparation was carried out by crushing and dispersing in ethanol. Finally, they were deposited onto carbon-coated copper grids.

Scanning electron microscopy (SEM) analyses were made on a JEOL 6400-LINK AN 10 000 microscope (Electron Microscopy Centre, UCM). The samples were prepared by placing them directly onto the holder and a posterior Au metallization.

A vibrating sample magnetometer (ISOM, UPM, Madrid) with a maximum applied continuous field of 10 000 Oe was used, at room temperature, to study the magnetic properties.

UV-vis spectroscopy was carried out in a UNICAM UV 500 spectrometer between 200 and 500 nm.

The size of magnetic nanoparticles in the ferrofluid and zeta potential of the samples dispersed in water was measured by means of a Zetasizer Nano ZS (Malvern Instruments) equipped with a 633 nm "red" laser.

**Calculation Procedures.** The surface area was determined using the Brunauer-Emmett-Teller (BET) method, evaluating the adsorption data in a relative pressure range  $p/p^0$  from 0.06 to 0.2. The pore volume,  $V_{\text{pore}}$  (cm<sup>3</sup>·g<sup>-1</sup>), was estimated from the amount of N<sub>2</sub> adsorbed at a relative pressure around 0.99. The pore size distribution between 0.5 and 40 nm was calculated from the desorption branch of the isotherm by means of the Barrett-Joyner-Halenda (BJH) method. The mesopore size,  $\Phi_{\text{pore}}$  (nm), was determined from the maximum of the pore size distribution curve. The pore wall thickness was evaluated as the difference between the unit cell parameter,  $a$ , and  $\Phi_{\text{pore}}$ , where  $a$  was calculated from the interplanar spacing ( $d$ ) of the (10) planes using the formula  $a = 2d(100)/\sqrt{3}$ .

## Results

Figure 1 displays a SEM micrograph of microspheres synthesized by the aerosol-assisted method. Specifically, the sample shown corresponds to MMS25. The spheres are

(58) Kokubo, T.; Kushitani, H.; Sakka, S.; Kitsugi, T.; Yamamuro, T. *J. Biomed. Mater. Res.* **1990**, *24*, 721.



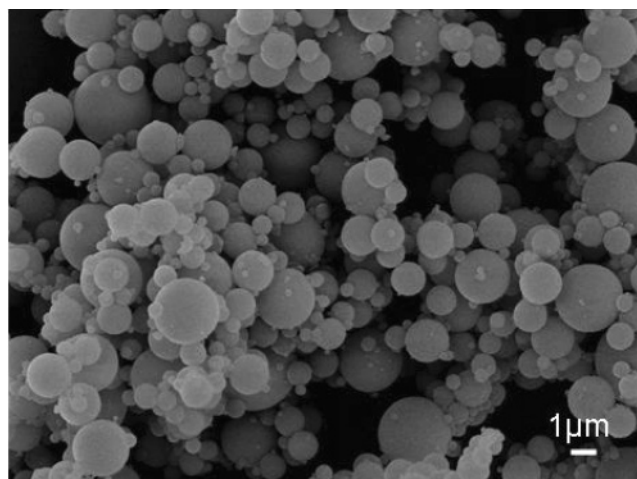


**Figure 1.** SEM micrograph of MMS25. Spheres synthesized with different amounts of surfactant and  $\gamma$ -Fe<sub>2</sub>O<sub>3</sub> nanoparticles do not show morphological differences. Magnification 5000 $\times$ .

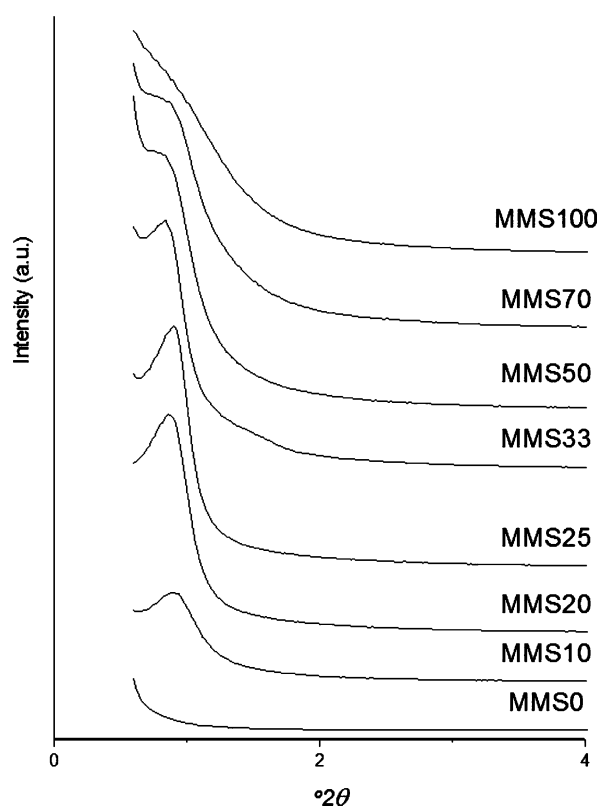


**Figure 2.** Small-angle XRD patterns of the materials prepared with varying P123/TEOS wt % ratio in the precursor solution.

heterogeneous in size with a diameter from 0.3 to 3  $\mu$ m. Their surface is smooth and no aggregation between them is observed. Spheres synthesized with different amounts of both surfactant and magnetic nanoparticles do not have either morphological or textural differences compared to those shown in Figure 1.

Figure 2 collects the small-angle XRD patterns of the spheres with different P123/TEOS ratio in the precursor solution. Samples synthesized with surfactant content from 10 to 33% (P123/TEOS) show a unique maximum with a  $d$ -spacing of 9.8 nm at around  $2\theta = 0.9^\circ$ , which can be assigned to the (10) reflection of a 2D-hexagonal ( $p6mm$ ) structure based on TEM observations, like that exhibited by

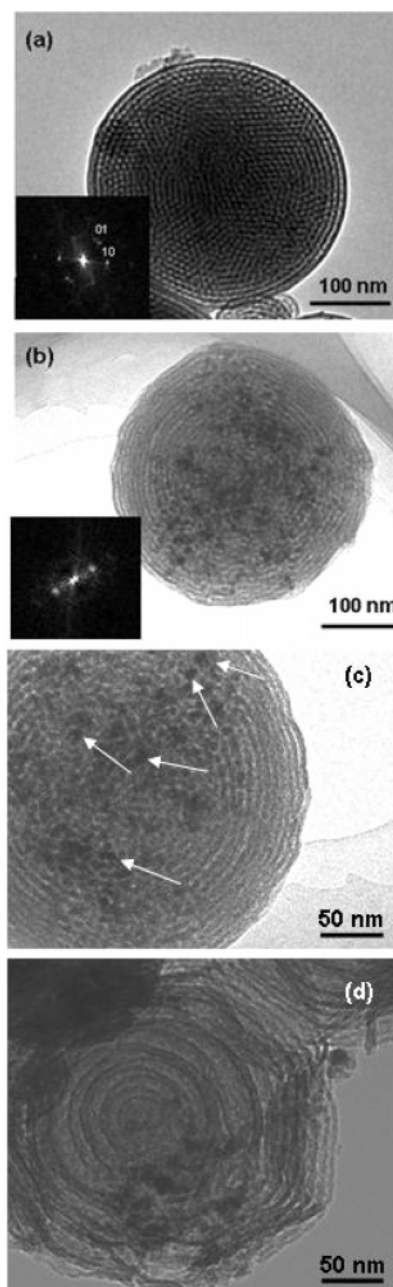


**Figure 3.** TEM images and FT diffractograms of the microspheres obtained from different phases. (a) 2D hexagonal (main phase), (b) lamellar (minor phase), and (c) magnification of (b) with pointed maghemite nanoparticles are micrographs of MMS25 (11). (d) Micrograph of sample MMS50.

a SBA-15 type material.<sup>59</sup> This maximum becomes broader in MMS 50, and it is not observed in MMS70 and MMS100 and in those materials synthesized in the absence of surfactant.

TEM images show that the MMS25 material is composed of two different phases. The main phase corresponds to 2D-hexagonal ( $p6mm$ ) spherical mesoporous particles (Figure 3a) and the minor phase corresponds to lamellar (onion-like) spherical mesoporous particles (Figure 3b). The dark contrast, highlighted in Figure 3c, can be assigned as Fe<sub>2</sub>O<sub>3</sub> nanoparticles from EDS analyses in both cases. Figure 3d shows a TEM image of a sample with high surfactant concentration

(59) Zhao, D.; Feng, J.; Huo, Q.; Melosh, N.; Fredrickson, G. H.; Chmelka, B. F.; Stucky, G. D. *Science* **1998**, 279, 548.

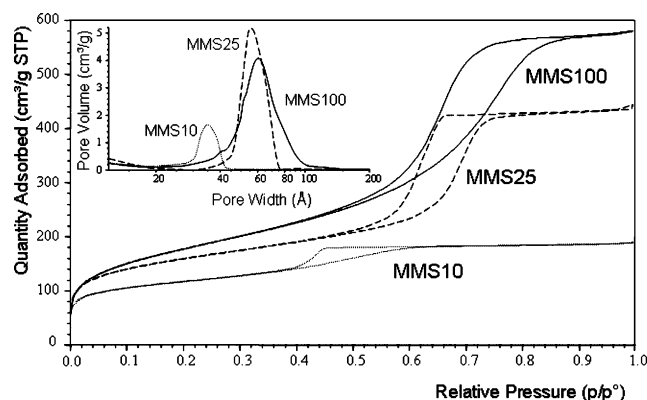


**Figure 4.**  $N_2$  sorption isotherms and pore size distributions of samples MMS100, MMS25, and MMS10.

**Table 1.** Textural Parameters Obtained by  $N_2$  Sorption Porosimetry for Some of the Samples Prepared with Varying P123/TEOS Ratio in the Precursor Solution

sample	$S_{\text{BET}}$ ( $\text{m}^2/\text{g}$ )	$V_{\text{pore}}$ ( $\text{cm}^3/\text{g}$ )	$\phi_{\text{pore}}$ (nm)
MMS100	645	0.9	6.2
MMS50	540	0.9	6.5
MMS25	566	0.7	5.6
MMS10	409	0.3	3.5

(MMS50). This sample displays a lamellar defective structure, exhibiting a loss of ordering with respect to MMS25.

Table 1 collects the textural parameters obtained by  $N_2$  adsorption porosimetry for the mesoporous spheres. Increases in BET surface areas (from 409 to  $645 \text{ m}^2 \cdot \text{g}^{-1}$ ), pore volumes (from 0.3 to  $0.9 \text{ cm}^3 \cdot \text{g}^{-1}$ ), and pore sizes (from 3.5 to 6.5 nm) are generally observed when the P123/ $\text{SiO}_2$  ratio is higher in the samples. The sorption isotherms and the pore size distributions of MMS100, MMS25, and MMS10 materials are displayed in Figure 4. According to the IUPAC, the isotherms of MMS100 and MMS25 can be classified as type IV with a H1 hysteresis loop, characteristic of mesoporous materials with pores opened at both ends and narrowings along the pore. MMS25 presents an isotherm essentially similar to that of MMS100 but with a decrease in the adsorption capacity. The isotherm of sample MMS10 evidences a low adsorption capacity, with a significant contribution of micropores, and a shift of the evaporation step to a lower relative pressure. H2 hysteresis loop is observed in this sample. All the materials show narrow and monomodal pore size distributions inside the range of mesopore.

As indicated by XRD and TEM results, MMS25 material presents the highest mesoporous ordering degree. For this reason, the surfactant-to-silica precursor ratio equal to 25 was selected for the synthesis of the second series of samples. In this series, the maghemite nanoparticles content in the material was varied. The samples were denoted as MMS25-( $x$ ), where  $x$ , as reported in the Experimental Section, indicates the  $\gamma\text{-Fe}_2\text{O}_3/\text{SiO}_2$  weight ratio in the final composition.

Figure 5 shows the small-angle XRD patterns of MMS25-type spheres with different amounts of  $\gamma\text{-Fe}_2\text{O}_3$  nanoparticles. A unique maximum can be distinguished at around  $2\theta = 0.9^\circ$  in samples MMS25(0), MMS25(11), and MMS25(25). It can be observed that this maximum is broader and less

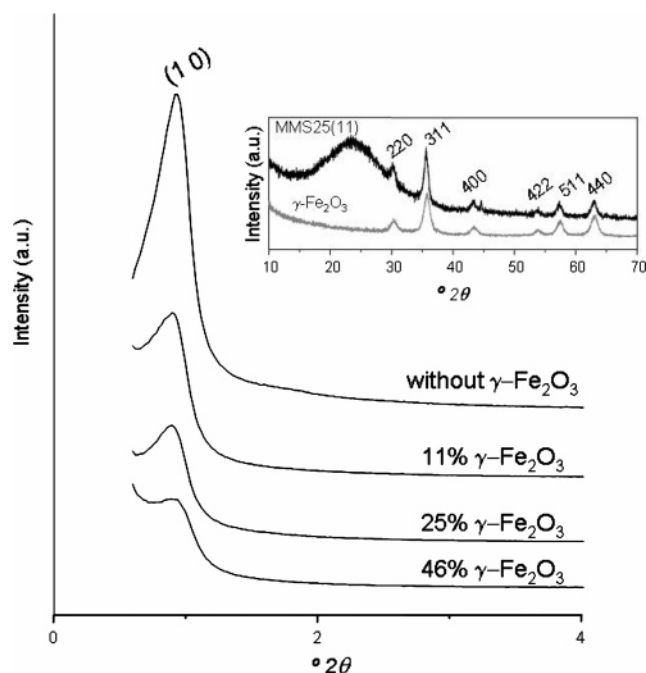


**Figure 5.** Small-angle XRD patterns of the materials prepared with a P123/TEOS wt % ratio equal to 25 and a varying  $\gamma\text{-Fe}_2\text{O}_3/\text{SiO}_2$  ratio in the final composition. The inset shows XRD patterns of bare  $\gamma\text{-Fe}_2\text{O}_3$  nanoparticles and MMS25(11).

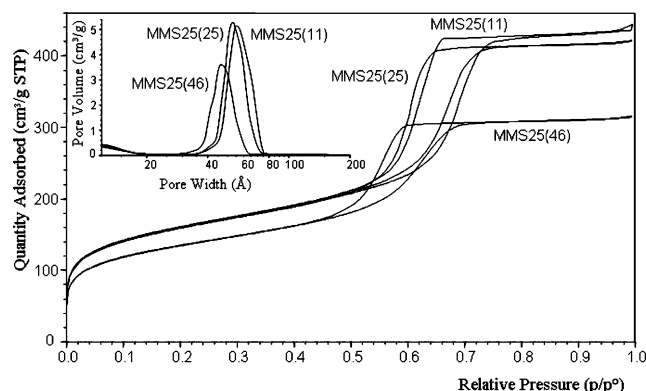


**Figure 6.**  $N_2$  sorption isotherms and pore size distributions of samples with different contents in  $\gamma\text{-Fe}_2\text{O}_3$  incorporated particles.

intense as the concentration of nanoparticles inside the spheres is higher.

The inset in Figure 5 compares a representative pattern of MMS samples in the  $2\theta$  range from  $10$  to  $70^\circ$  with that of bare maghemite nanoparticles added in the synthesis. All the maxima can be assigned to the reflections of a maghemite phase. The wideness of the reflections is characteristic of a nanocrystalline material. Microstructural features of  $\gamma\text{-Fe}_2\text{O}_3$  crystals were studied via full profile analysis after the Rietveld refinement of the XRD pattern with FullProf2000. Assuming an isotropic crystal growth (spherical nanoparticle), the average crystal size calculated was 5.7 nm, which is in accordance with TEM observations at higher magnification. Moreover, it should be noted that the maxima corresponding to the structure of paramagnetic hematite ( $\alpha\text{-Fe}_2\text{O}_3$ ) are not present in the diffractogram.

The  $N_2$  sorption isotherms and the pore size distributions of samples synthesized with different amounts of ferrofluid are depicted in Figure 6. Type IV isotherms and H1 type hysteresis loops are identified in all of them. Pore diameter

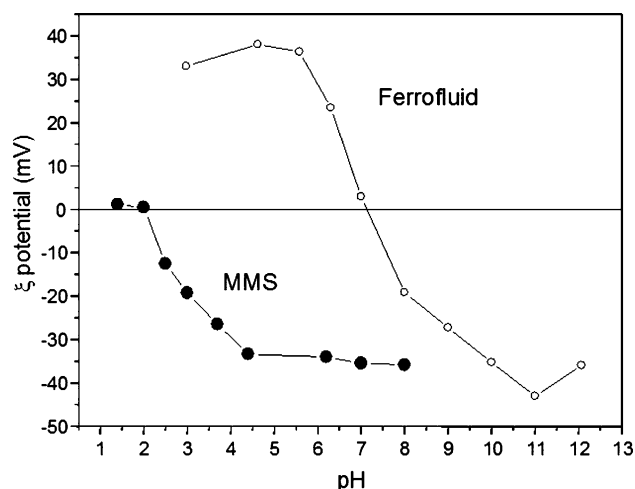


**Figure 7.** Zeta potential measurements of a representative MMS sample compared to the original ferrofluid as a function of pH.

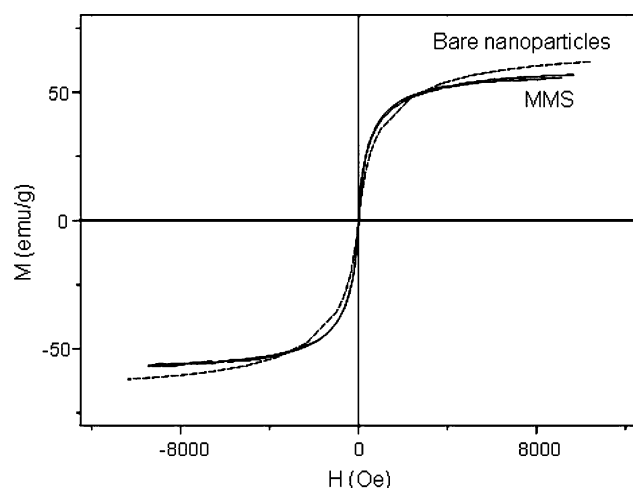


**Figure 8.** Magnetization curves of a representative MMS sample compared to the bare magnetic nanoparticles obtained from the ferrofluid under a maximum applied continuous magnetic field of 10000 Oe. Magnetization values have been normalized by the amount of maghemite in each sample.

(from 5.6 to 4.6 nm) and pore volume (from 0.7 to 0.5  $\text{cm}^3\cdot\text{g}^{-1}$ ) decreases are observed when the maghemite content is increased in the material. In the case of BET surface area, it remains constant ( $570 \text{ m}^2\cdot\text{g}^{-1}$ ) when the  $\gamma\text{-Fe}_2\text{O}_3/\text{SiO}_2$  ratio rises from 11% to 25%. However, the adsorption capacity is significantly reduced for the sample with 46% maghemite, for which surface area drops to  $479 \text{ m}^2\cdot\text{g}^{-1}$ .

Figure 7 shows the variation of zeta potential as a function of pH of a representative MMS sample. The isoelectric point of the curve is around pH 2. For comparison purposes, zeta potential measurements of corresponding bare magnetic nanoparticles are represented. In this case, the isoelectric point shifts toward neutral pH.

The results of the magnetic measurements are depicted in Figure 8. The magnetization curve of a representative MMS sample is compared to the bare magnetic nanoparticles obtained from the ferrofluid. The magnetization values, given in  $\text{emu}\cdot\text{g}^{-1}$ , of the representative MMS sample are referred to the  $\gamma\text{-Fe}_2\text{O}_3$  mass contained in the material, in this case 10 wt %. Then, saturation magnetization is equal to  $57 \text{ emu}\cdot\text{g}^{-1}$  for MMS, whereas the bare magnetic nanoparticles

reach  $62 \text{ emu}\cdot\text{g}^{-1}$ . Both curves are characteristic of superparamagnetic materials since they display no hysteresis.

Figure 9 summarizes both the textural and structural patterns of MMS25(11) before and after the loading with ibuprofen. Small-angle XRD patterns are shown in Figure 9A. It can be observed that the only maximum observed in MMS25(11) becomes less intense after the loading of the drug. The XRD patterns carried out in samples after compression (data not shown) display the same profile as those obtained in nonpressed materials. Thus, it is assumed that the mesostructure is not destroyed by pressing. Figure 9B shows the  $\text{N}_2$  sorption isotherms as well as the pore size distribution of the material before and after the loading, and it reveals that the surface area, the pore size, and the pore volume diminish when the drug is adsorbed into the spheres (from 566 to  $356 \text{ m}^2/\text{g}$ , from 5.6 to 4.8 nm, and from 0.7 to  $0.38 \text{ cm}^3/\text{g}$ , respectively). These results confirm that the MMS are incorporating ibuprofen inside the mesopores. Further TG analysis and CHN microanalysis revealed that the uptake amount of ibuprofen from the loading solution was 20%. Figure 9C shows that the particles loaded with ibuprofen can be totally separated from SBF under an external magnetic field.

The release behavior of ibuprofen from the materials can be studied in Figure 10. During the first hours, an immediate release (around 55%) of ibuprofen from the materials is observed. After this first “burst” effect, the drug is released in a more controlled fashion until the end of the essay.

## Discussion

The aerosol-assisted method described in the present work has demonstrated usefulness for the synthesis of silica-based magnetic mesoporous spheres. A homogeneous and stable precursor solution is necessary to achieve the formation of droplets of soluble silica, organic phase, and  $\gamma\text{-Fe}_2\text{O}_3$  nanoparticles. The characterization exposed in the present work has shown that magnetic nanoparticles are inside the microspheres and not as independent aggregates forming a separate phase. All the results confirm that the composition of the precursor solution allows the right assembly of all the components of the MMS.

Through a systematic study of the synthesis conditions, SEM indicates that the presence of  $\gamma\text{-Fe}_2\text{O}_3$  nanoparticles and the use of different amounts of surfactant have no influence in the size and morphology of MMS synthesized by the aerosol-assisted route. In all the cases, smooth, nonaggregated particles are obtained independently of the composition of the precursor solution.

From a structural point of view, an optimal range of concentrations of structure-directing agent in the precursor solution has been established for the synthesis of MMS with the aerosol-assisted method. According to XRD results, spheres with the highest degree of mesoporous ordering will be obtained when the % weight ratio of P123/TEOS is between 20 and 25. The formation of the mesostructured material is based on the evaporation of the solvent from the droplets inside the furnace. Thus, the concentration of surfactant inside the droplets will increase until it reaches and exceeds the critical micelle concentration (cmc). It is



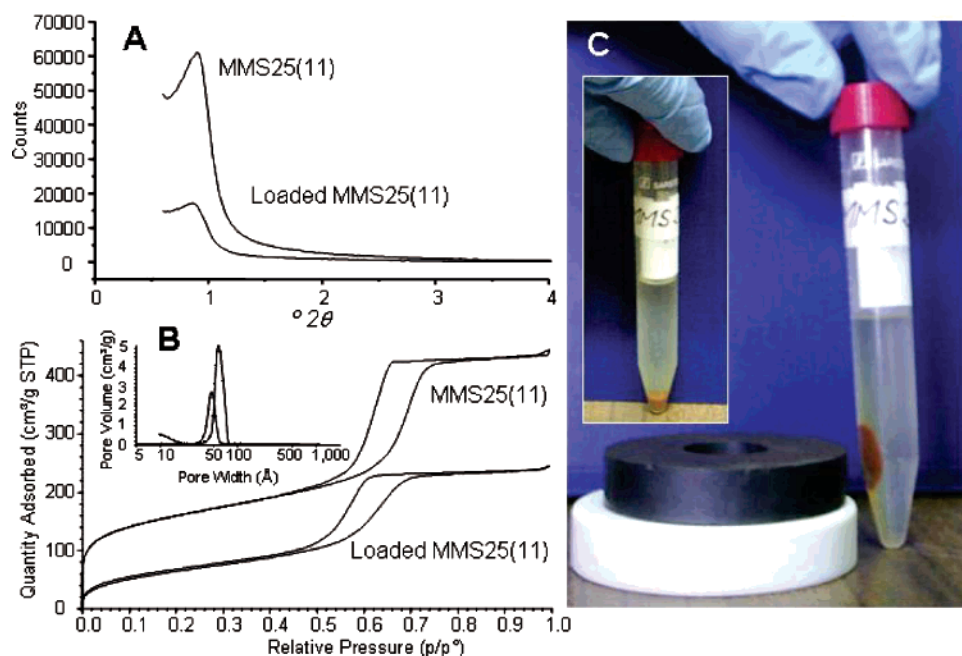


**Figure 9.** Small-angle XRD patterns (A), N<sub>2</sub> sorption isotherms and pore size distribution (B) of MMS25 before and after ibuprofen loading, and a photograph (C) showing the ability of drug-loaded material to be magnetically guided in SBF.

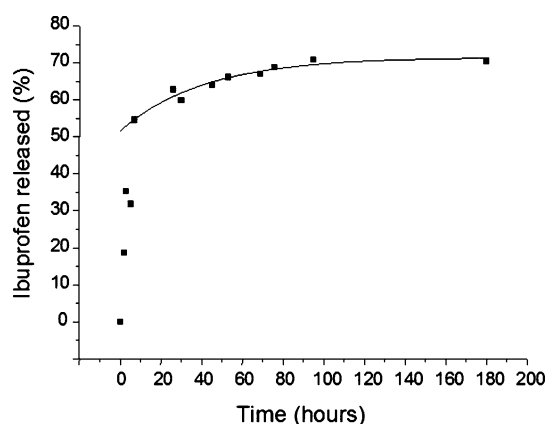


**Figure 10.** Percentage of ibuprofen released from loaded MMS25 as a function of time in an in vitro assay.

expected that above this cmc surfactant micelles will self-organize into different arrangements, from disordered to hexagonal, orthorhombic, cubic, or lamellar mesostructures depending on the final surfactant concentration. Nevertheless, this evolution is not observed in MMS where only disordered, hexagonal, or lamellar structures can be obtained. This anomaly, already observed by Brinker and co-workers<sup>50,60</sup> when using CTAB as the structure-directing agent, can be explained by the morphology of the final material. The high curvature imposed by the particles surface is altering the general packing behavior of the surfactant molecules<sup>61</sup> and so, for the case of P123 surfactant, only hexagonal and lamellar mesostructures can be obtained.

For higher surfactant concentrations the hexagonal symmetry is lost and a lamellar ordering takes place. It is well-known that lamellar structures are much weaker and after the thermal treatment collapse. Moreover, in this case, the

amount of silica in each droplet is lower as the surfactant amount increases, and consequently the silica wall thickness becomes thinner. After the thermal treatment, the final result is a defective structure, which shows a broad profile shoulder in XRD patterns and a poorly ordered lamellar structure by TEM observation.

The effect of the maghemite nanoparticles over the mesostructure has also been studied. Results obtained by small-angle XRD demonstrate that the presence of the  $\gamma$ -Fe<sub>2</sub>O<sub>3</sub> nanoparticles is influencing the final mesostructure of the materials, as the order of mesopore decreases when the concentration of maghemite is higher in the spheres. This observation is supported by the evolution of the textural properties, in which a high load of nanoparticles (46 wt %) leads to a decrease in the surface area and the pore volume.  $\gamma$ -Fe<sub>2</sub>O<sub>3</sub> nanoparticles, which are present during the formation of the mesophase, could avoid the correct interaction between the organic and the silica phases. This fact could be explained by two different mechanisms. On the one hand, magnetic nanoparticles could be interacting with the surfactant micelles. Nevertheless, it has been previously reported that iron oxide does not produce any chemical bonding with Pluronic surfactants.<sup>35</sup> On the other hand, the addition of iron oxide is leading to an increase of the inorganic/organic volume ratio in the mesophase and, as a result of this, it becomes defective. In any case, in the present work it is shown that despite the incorporation of a relatively high amount of  $\gamma$ -Fe<sub>2</sub>O<sub>3</sub> nanoparticles in the final material (such as 11%), well-ordered and magnetic mesostructures can be achieved.

XRD pattern is consistent with the presence of a nanocrystalline maghemite in the materials. Thus, the original nanoparticles in the ferrofluid have not changed during the synthesis of MMS. In addition, the formation of paramagnetic  $\alpha$ -Fe<sub>2</sub>O<sub>3</sub> was avoided in the process. This phase, which appears around 673 K, is considered an undesirable trans-

(60) Lu, Y.; Fan, H.; Stump, A.; Ward, T. L.; Rieker, T.; Brinker, C. J. *Nature* **1999**, 398, 223.

(61) Israelachvili, J. *Intermolecular and Surface Forces*; Academic Press: San Diego, CA, 1992.



formation of the added  $\gamma$ -Fe<sub>2</sub>O<sub>3</sub> since it causes the magnetic power to decrease. Some authors have reported the protective role of silica as an encapsulating matrix of iron oxide nanoparticles.<sup>62</sup> The fact that no hematite is formed during the synthesis is further proof of the incorporation of the maghemite nanoparticles into the silica network. It is also remarkable that the synthetic method used in our experiments has no effect on the crystallinity of the magnetic phase. As a result, the magnetic properties of the particles are not expected to vary.

The calculated pore wall thickness of the samples decreases from 7.9 to 4.0 nm as the P123/SiO<sub>2</sub> ratio is increased. The trends observed for the wall thickness and the textural parameters agree with those found in the literature for SBA-15 materials.<sup>63,64</sup> The sample of the series with the highest content in surfactant, MMS100, presents also the highest pore volume, 0.9 cm<sup>3</sup>·g<sup>-1</sup>. This fact suggests that the addition of surfactant is gradually increasing the porosity of the materials as a result of a more extended co-assembly of silica-surfactant mesophases. On the other hand, MMS10 textural properties seem not to be ruled by the surfactant. This sample presents a H2 hysteresis loop when studied by N<sub>2</sub> adsorption porosimetry, which indicates the presence of ink-bottle-like pores in the sample, characteristic of sol-gel silica.<sup>65</sup>

The isoelectric point indicates the pH at which the nanoparticles agglomerate, as a result of the loss of electrostatic repulsion. In the case of the ferrofluid, it is placed at pH 7, which makes the bare magnetic nanoparticles useless for operation at physiological conditions. In contrast, since the isoelectric point of silica is around pH 2, MMS possess a strongly negative surface charge around pH 7 ( $\xi = -35$  mV). This situation would allow our spheres to act as drug carriers at physiological pH.

MMS samples tested in this study have displayed superparamagnetic properties, in accordance with the small size of the magnetic cores embedded in the mesoporous spheres. The comparison between saturation magnetization values of MMS materials and the ferrofluid allows determination of the amount of magnetic nanoparticles encapsulated. In the case of MMS sample presented in Figure 8, it can be calculated that almost 92% of the maghemite nanoparticles added to the precursor solution have been placed inside the material. Therefore, it is assumed that the synthetic method employed in this work is suitable for the incorporation of magnetic nanoparticles into a mesoporous silica matrix. As expected, the magnetic nanoparticles thus keep their superparamagnetism after encapsulation. This superparamagnetic behavior is specially advantageous for hyperthermia, where the nanoparticles could generate heat as a result of a combination of Néel and Brownian mechanisms,<sup>19</sup> in addition to the drug targeting purpose.

With the in vitro drug release essay it has been shown that MMS are able to act as drug carriers. These materials can load a high amount of drug inside the mesoporous network and they can perform controlled delivery because of the confinement of the drug molecules in the ordered mesostructure. Drug release from MMS shows a first faster release, probably due to drug molecules associated to the outer surface. A slower release is observed afterward. This kind of kinetics is useful for those clinical cases that require a first high dose followed by a more stable dosage.

The drug incorporation was carried out by soaking the matrix into a highly concentrated drug solution and subsequent drying. Therefore, the process is mainly based on the adsorptive properties of mesoporous materials. During this process ibuprofen molecules get into the pores and remain adsorbed to the pore walls. The pore volume reduction evidences this situation. However, this adsorption is not the only site accessible to the ibuprofen molecules. The outer surface contains silanol groups able to retain ibuprofen molecules through hydrogen bonds and, moreover, ibuprofen molecules are expected to be also physisorbed at the outer surface. Both situations (ibuprofen inside and outside the pores) are compatible and neither excludes the other. Consequently, the release profile responds to a situation where more accessible molecules (outer ones) are promptly released, whereas those more deeply incorporated take longer times to diffuse at the environmental fluid.

From the point of view of the linkage between ibuprofen and the mesoporous matrix, it should be noted that ibuprofen has been incorporated to these systems on the assumption that its carboxyl group links the silanols at the surface. However, this situation is not exclusive, as the drug-drug interactions are also present and lead to ibuprofen dimers formation.<sup>10</sup> This dimer configuration is formed by an intermolecular hydrogen bond through the carboxyl groups and remains as physisorbed dimers on the surface, also explaining the predominant initial burst effect observed for these systems. It is well-known that drug delivery can be further controlled with chemical functionalization of the surface of the materials,<sup>66</sup> which is more interesting for systems intended as long-term delivery devices. This point is currently being studied by our research group.

## Conclusions

Silica mesoporous spheres containing magnetic nanoparticles have been synthesized following an aerosol-assisted method. The systematic study carried out in this work demonstrates that both the surfactant concentration and the amount of magnetic nanoparticles in the precursor solution affect the mesoscopic ordering degree of the materials. Magnetic nanoparticles undergo neither crystallinity changes nor superparamagnetic loss in the encapsulation process. In addition, the silica shell of these materials provides an appropriate surface to achieve stability at physiological pH. The combined properties of magnetic nanoparticles and silica microspheres make these materials excellent candidates for

(62) Mornet, S.; Grasset, F.; Portier, J.; Dugué, E. *Eur. Cells Mater.* **2002**, Suppl. 2, 110.

(63) Van der Voort, P.; Ravikovitch, P. I.; De Jong, K. P.; Neimark, A. V.; Janssen, A. H.; Benjelloun, M.; Van Bavel, E.; Cool, P.; Weckhuysen, B. M.; Vansant, E. F. *Chem. Commun.* **2002**, 1010.

(64) Choi, M.; Heo, W.; Kleitz, F.; Ryoo, R. *Chem. Commun.* **2003**, 1340.

(65) Balas, F.; Arcos, D.; Pérez-Pariente, J.; Vallet-Regí, M. *J. Mater. Res.* **2001**, 16, 1345.

(66) Balas, F.; Manzano, M.; Horcajada, P.; Vallet-Regí, M. *J. Am. Chem. Soc.* **2006**, 128, 8116.

biomedical applications that would involve hyperthermia treatments and drug delivery.

**Acknowledgment.** We are thankful for the financial support of CICYT Spain, through Research Project MAT2005-01486, CAM S-0505/MAT/000324. We also thank C. Aroca (ISOM-

UPM), F. Conde (C.A.I. X-ray Diffraction, UCM), E. Baldonado (Electron Microscopy Center, UCM), and C.A.I. Micro-analyses, UCM. Dr. Y. Sakamoto is also acknowledged for his valuable expert assistance during the manuscript discussion.

CM0705789